Mon. Not. R. Astron. Soc. **000**, 1–13 (2014) Printed 6 August 2014 (MN LATEX style file v2.2)

Constraints on the merging channel of massive galaxies since z∼1

I. Ferreras[1⋆], I. Trujillo[2,3], E. Mármol-Queraltó[2,3,4], P. G. Pérez-González[5], A. Cava[5,6], G. Barro[7], J. Cenarro[8], A. Hernán-Caballero[9], N. Cardiel[5], J. Rodríguez-Zaurín[2,3], M. Cebrián[2,3]

[1] *Mullard Space Science Laboratory, University College London, Holmbury St Mary, Dorking, Surrey RH5 6NT, UK*
[2] *Instituto de Astrofísica de Canarias, C/ Vía Láctea s/n, La Laguna, E-38200 La Laguna, Tenerife, Spain*
[3] *Departamento de Astrofísica, Universidad de La Laguna, E-38205 La Laguna, Tenerife, Spain*
[4] *Institute for Astronomy, University of Edinburgh, Royal Observatory, Blackford Hill, Edinburgh EH9 3HJ, UK*
[5] *Departamento de Astrofísica, Facultad de CC. Físicas, Universidad Complutense de Madrid, E-28040 Madrid, Spain*
[6] *Observatoire de Genève, Université de Genève, 51 Ch. des Maillettes, 1290 Versoix, Switzerland*
[7] *UCO/Lick Observatory, Department of Astronomy and Astrophysics, University of California, Santa Cruz, CA 95064, USA*
[8] *Centro de Estudios de Física del Cosmos de Aragón, Plaza San Juan 1, Planta 2, 44001 Teruel, Spain*
[9] *Instituto de Física de Cantabria, CSIC-UC, Avenida de los Castros s/n, E-39005 Santander, Spain*

Accepted 2014 July 15. Received 2014 June 11; in original form 2013 December 18

ABSTRACT

We probe the merging channel of massive galaxies over the z$= 0.3 - 1.3$ redshift window by studying close pairs in a sample of 238 galaxies with stellar mass $\gtrsim 10^{11}$M$_\odot$, from the SHARDS survey. SHARDS provides medium band photometry equivalent to low-resolution optical spectra (R∼50), allowing us to obtain extremely accurate photometric redshifts (median $|\Delta z|/(1+z) \sim 0.55\%$) and to improve the constraints on the age distribution of the stellar populations. Our dataset is volume-limited, probing merger progenitors with mass ratios 1:100 ($\mu \equiv M_{\rm sat}/M_{\rm cen} = 0.01$) out to z=1.3. A strong correlation is found between the age difference of host and companion galaxy and stellar mass ratio, from negligible age differences in major mergers to age differences ∼4 Gyr for 1:100 minor mergers. However, this correlation is simply a reflection of the mass-age trend in the general population. The dominant contributor to the growth of massive galaxies corresponds to mass ratios $\mu \gtrsim 0.3$, followed by a decrease in the fractional mass growth rate linearly proportional to $\log \mu$, at least down to $\mu \sim 0.01$, suggesting a decreasing role of mergers involving low-mass companions, especially if dynamical friction timescales are taken into account. A simple model results in an upper limit for the average mass growth rate of massive galaxies of $(\Delta M/M)/\Delta t \sim 0.08 \pm 0.02\,{\rm Gyr}^{-1}$, over the z $\lesssim 1$ range, with a $\sim 70\%$ fractional contribution from (major) mergers with $\mu \gtrsim 0.3$. The majority of the stellar mass contributed by mergers does not introduce significantly younger populations, in agreement with the small radial age gradients observed in present-day early-type galaxies.

Key words: galaxies: evolution – galaxies: formation – galaxies: interactions – galaxies: high-redshift

1 INTRODUCTION

One of the possible scenarios for the formation and evolution of the quiescent massive galaxies at low-redshift posits that after forming the core of their structures in an early dissipative event at high redshift (z $\gtrsim 2$), these galaxies continue growing in mass and size due to a continuous infall of material (see, e.g., Naab et al. 2009). In this picture, the main channel of growth is provided by mergers with companion galaxies having a mass ratio 1:5 (Oser et al. 2012). The homogeneous age distribution of massive galaxies out to z∼1 (Ferreras et al. 2005, 2009a,b) reveals that these mergers must be relatively gas poor, without any significant star formation (Pérez-González et al. 2008; Trujillo et al. 2011). Numerical simulations suggest that the stellar content of this accreted material should be mainly deposited in the outer regions of the massive galaxy, with ages around 2.5 Gyr older than the component formed in-situ (Lackner et al. 2012). Observational evidence of minor merger progenitors – loosely defined as those where the stellar mass ratio between host and companion is lower than 1:4 – is found in various systems, including stellar streams in the Milky Way (e.g., Bell et al. 2008), and the presence of residual star formation in nearby early-type galaxies (Kaviraj et al. 2007). Although

⋆ Email: i.ferreras@ucl.ac.uk

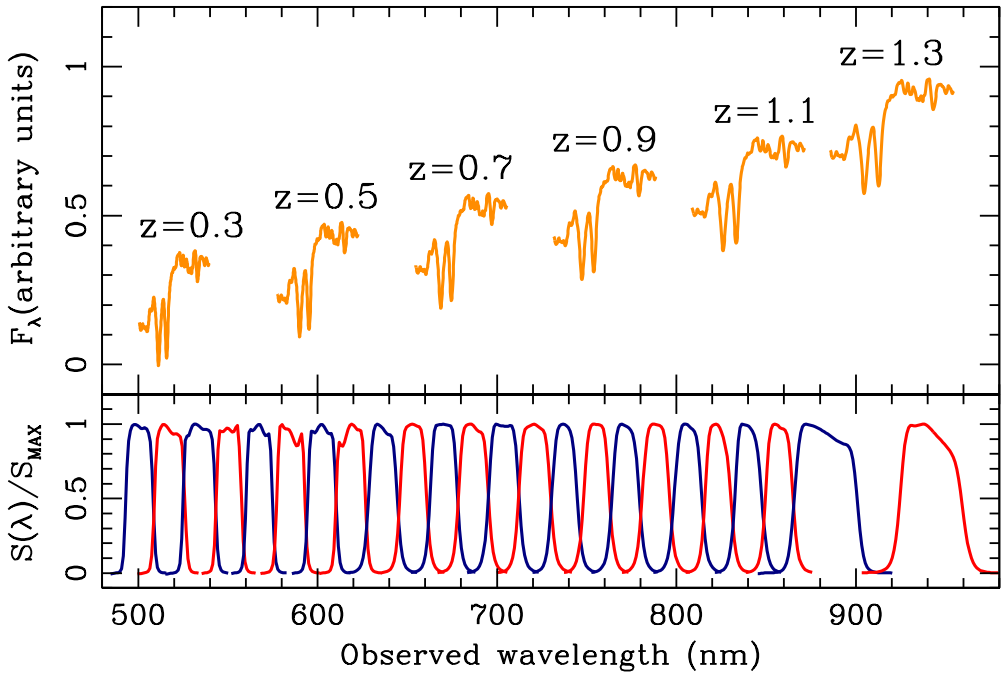

Figure 1. The spectral response of the SHARDS filters available for this study are shown (bottom, normalized in each case to the peak of the response). The upper panel shows the typical spectrum of an evolved stellar population around the age-sensitive 4000Å break, for a number of redshift values representative of our sample.

several pieces of observational evidence favour the above depicted scenario, the role of minor mergers on the growth of massive galaxies is still poorly constrained.

In the z∼0 Universe, the aftermath of merging activity can be assessed via ultra-deep photometry and spectroscopy, probing the radial gradients of the properties of stellar populations (see, e.g., Sánchez-Blázquez et al. 2007). However, the interpretation is hard because of the challenging observations, the difficulty in circumventing the age-metallicity degeneracy inherent in old stellar populations, and the added complication of the presence of a halo of old, metal-poor stars at galactocentric distances $R \gtrsim 4-8R_e$ (La Barbera et al. 2012). In fact, detailed surface brightness analyses of nearby massive early-type galaxies reveal a complex structure, where at least three components can be discerned: a compact core; an intermediate region, and an outer halo (Huang et al. 2013; Montes et al. 2014). Separating these components in nearby systems to derive the assembly history poses a serious challenge. Alternatively, it is possible to explore at high redshift the stellar population properties of close pairs of galaxies involving a massive galaxy (host) and a satellite (companion) that will eventually collapse into the main body. This is the approach followed in this paper. In contrast with studies where the selection of merger progenitors is based on morphological features (see, e.g., Conselice 2006; Lotz et al. 2011; Bluck et al. 2012), our selection is based on targeting pairs of galaxies with a small projected separation *and* located at the same redshift, a more conservative approach (see, e.g. Patton et al. 2000; Rogers et al. 2009; Lin et al. 2010; López-Sanjuan et al. 2011), however, requiring accurate redshift estimates. In Mármol-Queraltó et al. (2012, 2013), a sample of massive galaxies out to $z \lesssim 2$ was studied, finding a constant fraction (∼30%) of massive galaxies with one, or more, satellites and younger stellar populations in the satellites with respect to the centrals. However, this sample was limited by the uncertainties in the photometric redshift estimates based on broadband photometry – at the level of $|\Delta z|/(1+z) = 5\%$. This paper extends this work in two ways: Firstly by the use of improved photometric data that allows for photometric redshifts that are an order of magnitude more accurate. Secondly, the data provides low-resolution photo-spectra, resulting in better constraints on the age of the underlying stellar populations of host and companion in merger progenitors.

The Survey for High-z Absorption Red and Dead Sources (hereafter SHARDS, Pérez-González et al. 2013) comprises ultra-deep optical spectro-photometric observations acquired at the 10.4m Gran Telescopio Canarias (GTC) that provide an effective spectral resolution $R = \lambda/\Delta\lambda \sim 50$, with a set of 24 medium band filters. This survey enables us to obtain accurate redshifts and to probe the underlying stellar populations. We use here the SHARDS data to define a sample of massive galaxies, with a robust characterization of nearby companions as merger progenitors, allowing us to constrain in detail the merging channel of massive galaxies since z∼1. This paper is structured as follows: In Section 2, we present the sample of massive galaxies and the selection of host-companion pairs, including a description of the methodology followed to obtain accurate photometric redshifts, and the derivation of stellar ages. Section 3 compares the distribution of the ages of the underlying stellar populations, followed by an estimate, in Sec. 4, of the contribution in mass of these satellites to the growth of massive galaxies. Finally, Sec. 5 gives an overview of our conclusions. Throughout this paper, a standard ΛCDM cosmology is adopted: $\Omega_m = 0.3$, $\Omega_\Lambda = 0.7$, $H_0 = 70\,\mathrm{km\,s^{-1}\,Mpc^{-1}}$ (or, equivalently, $h_{70} = 1$).

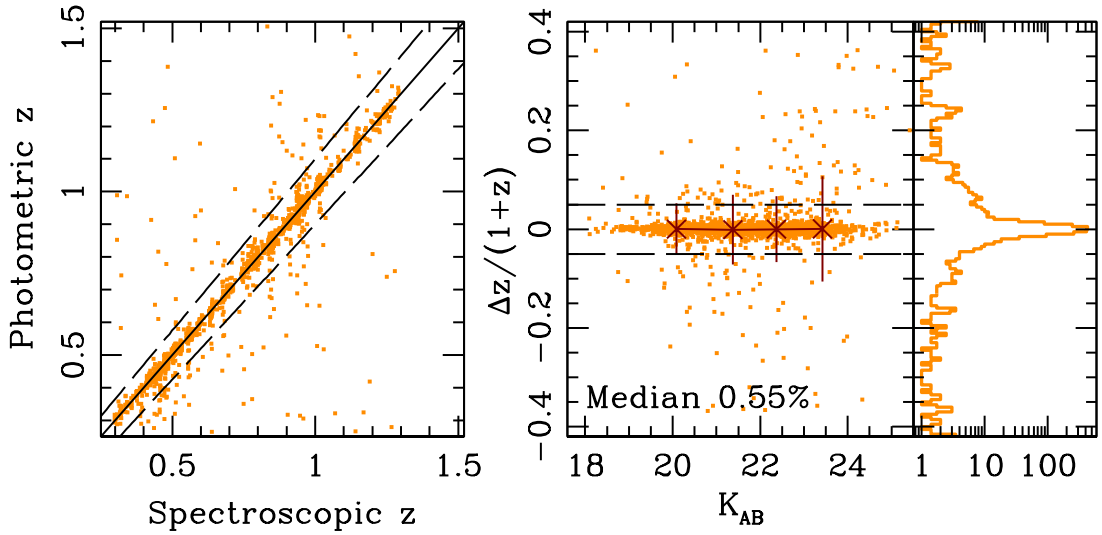

Figure 2. *Left:* Comparison of photometric and spectroscopic redshifts for a subsample of 2792 galaxies with available spectroscopic data. The solid and dashed lines represent the 1:1 correspondence, and an uncertainty of 5%, respectively. *Right:* The accuracy in the photometric redshifts is shown as a function of the total apparent K-band magnitude, including the same 5% interval as a dashed line (typical of standard photometric redshifts with broadband photometry alone). The rightmost panel shows the distribution of the photometric redshift accuracy in SHARDS.

2 SAMPLE SELECTION

2.1 Datasets

SHARDS provides deep imaging (m<26.5 AB at the $3\,\sigma$ level) in a number of contiguous, medium band filters towards the GOODS-N region, over a 130 arcmin^2 field of view, split into two pointings. The survey covers a 500–950 nm spectral range in 24 medium-band filters (FWHM=15 nm, except for the two reddest ones, with FWHM=30 nm). Tab. 1 gives an overview of the SHARDS filters used and the depth and seeing of the observations (see Pérez-González et al. 2013, for details). The main science driver of the SHARDS survey is the characterization of the stellar populations of massive galaxies at z>1 by use of the Mg_{UV} spectral feature (Pérez-González et al. 2013; Daddi et al. 2005). However, the data set also provides information of the age-sensitive region around the 4000 Å break at moderate redshift (see Fig. 1). In Hernán-Caballero et al. (2013) the SHARDS data were used to analyze the D4000 index (see, e.g., Balogh et al. 1999) at z<1.1. In this paper we concentrate on the characterization of the close companions of massive galaxies using the medium band photometry to secure accurate photometric redshifts and to assess the age of the underlying stellar populations by way of spectral fitting at a low spectral resolution. We find that the optimal redshift range to extract stellar ages using the spectral window around the 4000Å break corresponds to $0.3 \lesssim z \lesssim 1.3$, covering 5.3 Gyr of cosmic time. Within the adopted cosmology, this sample covers a total comoving volume of $2.24 \times 10^5 h_{70}^{-3}$Mpc^3.

In addition to the SHARDS data, we include the matched photometry from the IRAC-selected ($[3.6\mu m]_{AB} < 24$) catalogue of Pérez-González et al. (2008b) sources, for which UV to IR fluxes are available. Photometry in all UV-to-NIR bands was performed in elliptical Kron (1980) apertures. The best aperture was obtained for each galaxy by averaging the values in the different bands, always imposing a minimum semi-major axis equal to the worst seeing in our dataset (1.1 arcsec). Fluxes for the IRAC bands were measured

Table 1. Characteristics of the SHARDS filter set and observations. CWL is the central wavelength (in nm) of the filter for an angle of incidence AOI=10.5° (approximately that for the center of the FOV). The width of the filter is given as the FWHM of the response curve. $m_{3\sigma}$ is the sensitivity limit, quoted at the $3\,\sigma$ level (AB mag). The average seeing is given in the last columns. P1 and P2 represent the individual pointings of the SHARDS observations.

Filter	CWL nm	Width nm	$m_{3\sigma}$ AB		seeing arcsec	
			P1	P2	P1	P2
F500W17	500.8	13.7	27.34	27.46	0.96	0.94
F517W17	519.7	14.6	27.16	27.42	0.79	0.93
F534W17	536.3	16.4	27.26	27.30	0.92	0.81
F551W17	552.1	12.3	27.15	27.19	0.83	0.78
F568W17	568.9	13.5	27.06	27.17	0.83	0.82
F585W17	586.5	14.0	27.15	27.24	0.97	0.89
F602W17	603.0	14.5	27.07	27.18	0.88	0.89
F619W17	618.9	14.8	27.06	27.18	0.85	0.90
F636W17	638.4	15.1	27.03	27.12	0.80	0.93
F653W17	653.1	14.6	27.09	27.15	0.98	1.00
F670W17	668.4	15.0	26.97	27.17	0.79	1.08
F687W17	688.2	15.1	26.98	27.04	0.83	0.90
F704W17	704.5	16.9	26.92	26.99	0.89	0.93
F721W17	720.2	18.0	26.88	26.94	0.94	1.02
F738W17	737.8	14.8	26.86	26.91	0.86	0.89
F755W17	754.5	14.6	26.87	26.90	0.93	0.94
F772W17	770.9	15.1	26.90	26.89	0.94	1.08
F789W17	789.0	15.3	26.79	26.84	0.96	0.93
F806W17	805.7	15.4	26.95	26.86	0.97	1.00
F823W17	825.4	14.5	26.88	26.81	0.82	0.96
F840W17	840.0	15.1	26.75	26.73	0.94	0.97
F857W17	856.4	15.4	26.88	26.77	0.73	0.98
F883W35	880.3	30.8	26.86	26.77	0.96	1.00
F941W33	941.0	30.0	26.63	26.64	0.91	0.95

within a 2 arcsec radius circular aperture, applying an aperture correction for isolated sources. For sources with companions closer than 2 arcsec (roughly the FWHM of the IRAC PSF), a deconvolution algorithm was applied, as explained in Barro et al. (2011) The ground-based NIR photometry, adopted from an update of the compilation of Pérez-González et al. (2008b), is taken from the deep observations of GOODS-N at Subaru/MOIRCS (Ichikawa et al. 2007) and CFHT/WIRCam (Wang et al. 2010), for which a 5σ detection limit of $K_{\rm AB} < 24.5$ is reached. In addition, we use the WFC3 NIR photometry in the Y (F105W), J (F125W) and H (F160W) bands from the CANDELS survey ($\rm H_{AB}(5\,\sigma) < 27$, Grogin et al. 2011; Koekemoer et al. 2011).

2.2 SED Fitting: Photometric redshifts

Photometric redshifts were estimated with the EAZY software (Brammer et al. 2008), using the templates tweaked for emission-line galaxies and medium-band photometry released in version 1.1. We fitted the available SEDs covering the wavelength range between the UV and the MIR, including the SHARDS data. The medium band filters enable us to obtain more accurate redshifts with respect to those based on broadband photometry. In Pérez-González et al. (2013), we discussed in detail a unique characteristic of our data: for observations using a given filter, the passband varies along the FOV of the GTC/OSIRIS instrument (resulting in a shift of the effective central wavelength, but keeping the shape constant). Hence, each galaxy in a SHARDS image "sees" a different passband. In order to take into account the variation of the central wavelength of the passband, a different execution of EAZY was carried out for each individual galaxy, setting the filter transmission files to the appropriate central wavelengths. This procedure was essential to derive accurate photometric redshifts. In fact, the estimates were a factor of 10 less precise when the shifts were not taken into account. A more detailed description of the method and results to estimate photometric redshifts will be presented in a future paper (Pérez-González et al. 2014, in preparation). Given that this paper focuses on the study of massive galaxies and their companions at z $\lesssim$ 1.3, we give photometric redshift quality figures only within this redshift range.

Fig. 2 shows the accuracy of our photometric redshift catalogue, for a subsample of 2,792 galaxies with available spectroscopic redshifts from the literature (down to $I \sim$25, see, e.g., Cowie et al. 2004; Wirth et al. 2004; Cooper et al. 2012). Over the 0.3<z<1.3 range covered in this paper, accurate photometric redshifts are obtained, largely due to the presence of the prominent 4000 Å break within the spectral coverage of the medium-band filter (see Fig. 1). The left-hand panel of Fig. 2 compares spectroscopic versus photometric redshift, with the solid line tracking a 1:1 correspondence, and the dashed lines spanning a 5% uncertainty, typical of standard photometric redshifts involving broadband data (e.g. Pérez-González et al. 2008b). The right-hand panel shows the photo-z accuracy with respect to total K-band magnitude, and the histogram with the narrow distribution. Note we use a logarithmic axis since the accuracy results in a highly peaked histogram on a linear scale. The dots represent individual galaxies, and the red crosses are binned estimates (at a fixed number of galaxies per bin), including the RMS within each bin as an error bar. The median of the distribution of $|\Delta z|/(1+z)$ is 0.55%, with a 1.6% fraction of catastrophic failures, using a very conservative definition, as those redshift estimates with an accuracy outside of $3\times$ the RMS of the distribution.

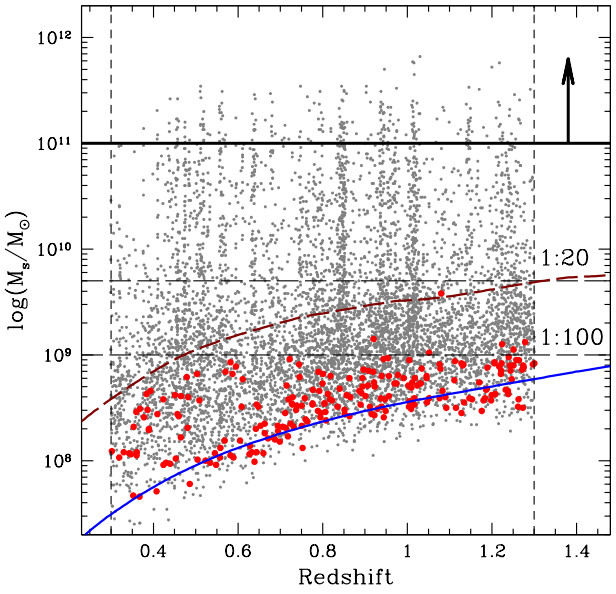

Figure 3. Stellar mass vs redshift diagram of the SHARDS sources used in this paper. A galaxy is classified as massive if the stellar mass is $\rm M_s > 10^{11}\,M_\odot$ (arrow and thick horizontal line). The horizontal dashed lines show the limit for 1:20 and 1:100 merger progenitors. The blue solid line shows a $K_{\rm AB} = 25$ simple stellar population with age 100 Myr, whereas the red dashed line corresponds to a $K_{\rm AB} = 25$ population formed at $z_{\rm FOR} = 3$ (both at solar metallicity, Chabrier IMF, using the models of Bruzual & Charlot 2003). The red dots correspond to sources with $\rm K_{AB} \sim$25.

2.3 SED Fitting: Stellar population properties

We model the SED of the parent sample using stellar population synthesis models to determine their stellar properties, primarily stellar masses and ages. These are critical for the selection of the main sample of massive galaxies and to analyze the age differences between them and their close companions. Briefly, the method involves a comparison of the SHARDS medium-band photometry with a large volume of composite models derived from the stellar population synthesis library of Bruzual & Charlot (2003) – a Chabrier (2003) stellar initial mass function (IMF) is assumed throughout this paper. Although recent claims suggest a more bottom-heavy IMF in massive galaxies (see, e.g., Cenarro et al. 2003; van Dokkum & Conroy 2010; Ferreras et al. 2013), its effect on the stellar M/L, and therefore on the stellar masses derived from the photometry, may not be as important, except for systems with very high velocity dispersion (La Barbera et al. 2013; Läsker et al. 2013).

Three sets of model grids are considered, comprising simple stellar populations (i.e. a single burst population); an exponentially decaying star formation history (τ model), or a constant star formation truncated after a timescale chosen as a free parameter. In addition to the continuum from the stellar population synthesis models, we include emission lines corresponding to a HII region (Aller 1984). The weighting of the emission line spectrum is parameterised by the equivalent width of the [O II] line. We note that the nebular continuum is neglected here, since we are dealing with a general sample of galaxies, where luminosity-weighted ages are always older than 0.1 Gyr. The contribution from the nebular continuum at those ages is expected to be negligible

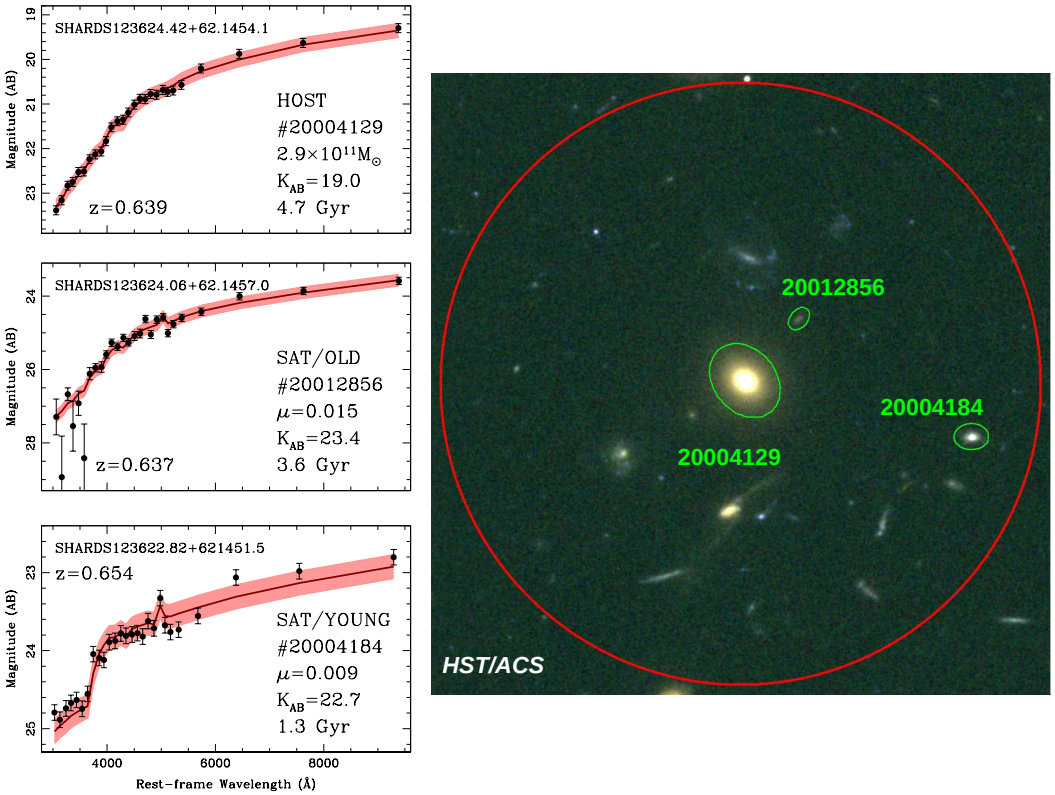

Figure 5. Example of a system with SEDs and best fit. The host is massive galaxy SHARDS123624.42+621454 (z=0.639, $M_s = 2.9 \times 10^{11} M_\odot$). The 30×30 arcsec^2 image (*right*) is an RGB colour composite from the GOODS-N *HST/ACS* archival data through the F606W, F775W, and F850LP passbands. The red circumference extends over the $100 h_{70}^{-1}$ kpc search radius. On the left, the observed data points (black circles) are compared with the best fit models (red lines). Each galaxy is labelled by its SHARDS ID, $K_{\rm AB}$ apparent magnitude, best-fit stellar age, and either stellar mass (host) or mass ratio (companion).

Table 2. Parameters defining the model grids for the analysis of stellar ages, based on Bruzual & Charlot (2003) models, and dust extinction from Cardelli et al. (1989).

Parameter	Symbol	Range	N
SIMPLE STELLAR POPULATIONS (SSP)			
Metallicity	$\log Z/Z_\odot$	$[-2.0, +0.3]$	6
Age	$\log t/{\rm Gyr}$	$[-2, \log t_U/{\rm Gyr}]$	64
Emission Lines	EW([O II])	$[0, 30]$ Å	12
Dust Reddening	E(B–V)	$[0, 0.5]$	12
τ MODELS (τSF)			
Metallicity	$\log Z/Z_\odot$	$[-2.0, +0.3]$	6
SF timescale	$\log \tau_{\rm SF}/{\rm Gyr}$	$[-1, 1]$	16
Formation epoch	$t_{\rm FOR}/t_U$	[0,1)	16
Emission Lines	EW([O II])	$[0, 30]$ Å	12
Dust Reddening	E(B–V)	$[0, 0.5]$	12
CONSTANT SF MODELS (CST)			
Metallicity	$\log Z/Z_\odot$	$[-2.0, +0.3]$	6
Truncation timescale	$\log \tau_t/{\rm Gyr}$	$[-1, 1]$	16
Formation epoch	$t_{\rm FOR}/t_U$	[0,1)	16
Emission Lines	EW([O II])	$[0, 30]$ Å	12
Dust Reddening	E(B–V)	$[0, 0.5]$	12
		Total Models	497,664

t_U is the age of the Universe at the redshift of the galaxy under study.

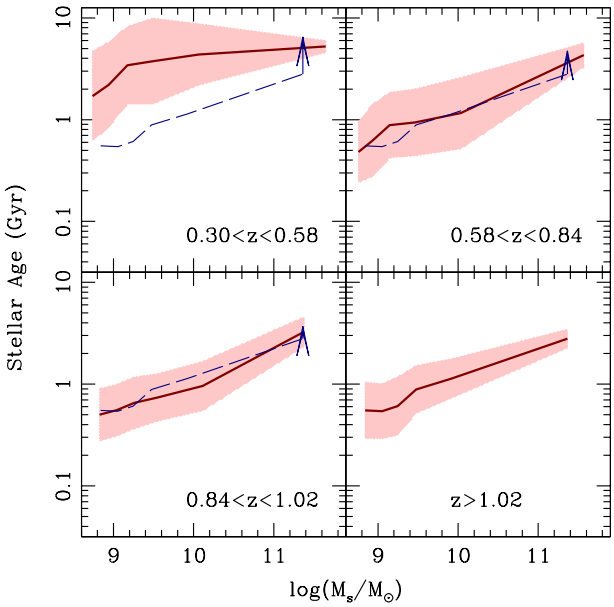

Figure 4. Mass-age relationship split into quartiles in redshift. The red lines and shading give the median and RMS scatter, respectively. The dashed lines give, for reference, the mass-age relation in the highest redshift bin. The arrows at the massive end correspond to the cosmic time spanned between the different redshift bins.

(Anders & Fritze-von Alvensleben 2003). The models are also subject to a Milky Way-type extinction, following the prescription of Cardelli et al. (1989). The range of parameters used in the definition of the templates are summarised in Tab. 2. The library of nearly half a million templates is integrated with the response of all the available filters, including a number of wavelength offsets in steps of 50Å (smaller changes in central wavelength cause variations at a much lower level than the photometric uncertainties). These offsets are needed to take into account the variation of the central wavelength of the filter with respect to the position of the source on the field of view (see Pérez-González et al. 2013, for details). For each galaxy, all models are run for the specific redshift and SHARDS filter offsets (which are unique for each galaxy and depend of the position of the image with respect to the optical axis), and compared with the observed fluxes measured in the SHARDS data. The comparison is used to derive a standard χ^2 statistic. A probability distribution function for the parameters is extracted from the χ^2-derived likelihood – i.e. $\mathcal{P} \propto \exp(-\frac{1}{2}\Delta\chi^2)$. For the type of sampling explored in this paper – where the number of gridpoints has to be constrained – probability-weighted values give more robust estimations than the actual gridpoint where the highest value of the likelihood is reached. Hereafter, all best-fit parameters are quoted as probability-weighted quantities. We emphasize that although this method is fairly rigid in terms of the star formation histories allowed, it is much more robust than spectral fitting methods based on partial searches of parameter space, such as the Monte Carlo Markov Chain approach (see, e.g., Cid Fernandes et al. 2005). We performed 500 simulations of arbitrary star formation histories to check that our retrieved ages were consistent within the error bars with the input values. Hereafter, stellar age is weighted with respect to the star formation rate, $\psi(t)$, namely:

$$\mathrm{Age} \equiv \langle \mathrm{Age} \rangle_\psi = \frac{\int [t_U(z) - t]\psi(t)dt}{\int \psi(t)dt}, \quad (1)$$

where the integrals extend between the formation time, $t_{\rm FOR}$, and the age of the Universe at the redshift of the galaxy, $t_U(z)$. We note that the age difference between SSP, τ and constant SF models is rather small: the difference $\Delta \equiv \log(\mathrm{Age}_{\rm CST}) - \log(\mathrm{Age}_{\rm SSP})$ is $\Delta = 0.14 \pm 0.84$ (1σ) for all galaxies, and $\Delta = 0.07 \pm 0.43$ for massive galaxies. In the Appendix we elaborate on the comparison between the age estimates according to these models, confirming that the trends found do not depend on the parameterisation of the star formation histories. Hereafter, the quoted ages and stellar masses correspond to those derived from the τ models.

2.4 Sample Selection

Based on the best-fit stellar masses obtained from the modelling of the stellar populations, we define our sample of (host) massive galaxies as those systems with stellar mass $M_s \geqslant 10^{11} M_\odot$. To determine the range of mass ratios between host and companion, we estimate the completeness level of the parent catalogue as a function of stellar mass. Fig. 3 shows the distribution of stellar mass over the redshift range under consideration (vertical dashed lines). To assess the completeness level, we compare our sample with synthetic models that have an apparent magnitude $K_{\rm AB} = 25$ (i.e. close to the limit of our sample). The dashed red line traces an old population formed at $z_{\rm FOR} = 3$, whereas the blue line corresponds to a 100 Myr age. We infer a very conservative completeness limit at a mass ratio of 1:20 if a wide range of stellar ages are considered. Due to the strong correlation between age and stellar mass found in galaxies over a wide redshift range (see, e.g., Pérez-González et al. 2008), we also propose a more realistic limit of 1:100. The red dots are real data at the chosen limit of $K_{\rm AB} = 25$, illustrating the fact that most of these galaxies have young stellar ages.

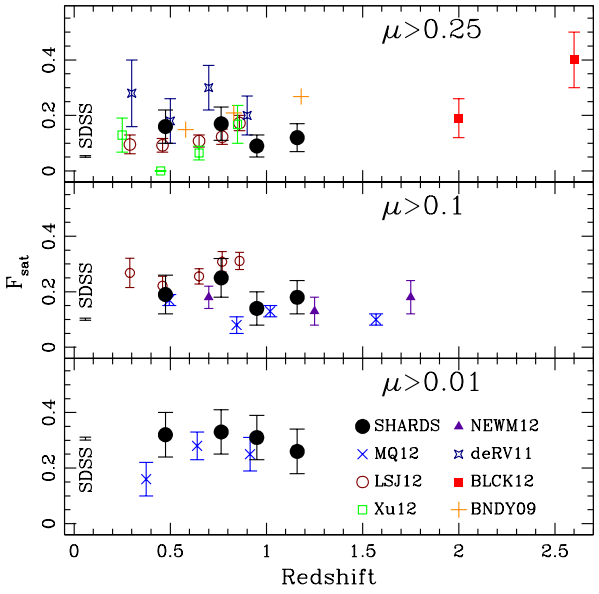

Figure 6. Redshift evolution of the fraction of close companions of massive galaxies ($M_s > 10^{11} M_\odot$), for three choices of the stellar mass ratio between satellite and central (μ). Our results (solid circles, SHARDS) are compared with recent results from the literature: Mármol-Queraltó et al. (2012, 'x' signs, MQ12); Ruiz et al. (in preparation, estimates at z=0, labelled 'SDSS'); López-Sanjuan et al. (2012, open circles, LSJ12); Xu et al. (2012, open squares, Xu12); Newman et al. (2012, triangles, NEWM12); de Ravel et al. (2011, stars, deRV11); Bluck et al. (2012, filled squares, BLCK12); Bundy et al. (2009, '+' signs, BNDY09).

Given the strong colour (i.e. star formation rate/age) bimodality as a function of stellar mass (i.e. red sequence vs. blue cloud, see, e.g., Bell et al. 2003; Baldry et al. 2004; Faber et al. 2007; Arnouts et al. 2007; Brammer et al. 2011), we expect the low-mass companions to be young (blue) star-forming systems. To illustrate and quantify this point, Fig. 4 plots the distribution of stellar age against mass for the whole sample. The data are binned in four redshift intervals. The lines and shaded regions trace the median and RMS scatter, respectively. Note the strong age-mass correlation, and its evolution with redshift. The dashed lines overlay the mass-age relation from the highest redshift bin, with the vertical arrows extending over the difference in cosmic time between redshift bins. These arrows confirm that passive evolution is the main driver of the photometric properties of massive galaxies at $z \lesssim 1$. Fig. 4 shows that for systems that would correspond to merger progenitors with a mass ratio below 1:20 (i.e. concerning companions at the low-mass end of the sample), we should not expect *old* ($\gtrsim 3-4$ Gyr) populations in the companions. In fact, for redshifts above the median value of the sample (z>0.85), the fraction of $M_s < 5 \times 10^9 M_\odot$ galaxies with ages older than 3 Gyr (2 Gyr) is just 0.14% (0.90%). In Sec. 4 we explore the completeness of the sample in more detail.

We note that the present analysis is mainly geared towards the determination of stellar ages. The models give significantly more accurate error bars in age than metallicity: only six independent

Table 3. Fraction of massive galaxies with close companions at various redshifts. For each redshift bin, $N_{\rm cen}$ is the total number of massive (central) galaxies; $F_{\rm obs}$ is the observed fraction of those with nearby sources. A simulation to correct for chance alignments due to the uncertainty in the estimates of redshift is given by $S_{\rm simul}$; with the corrected fraction being $F_{\rm sat}$. A final correction, $S_{\rm clust}$ has to be made to account for galaxy clustering. The final, corrected fraction of satellites is given by the last column, $F_{\rm sat,clust}$ (see text for details).

Redshift range	$N_{\rm cen}$	$F_{\rm obs}$	$S_{\rm simul}$	$F_{\rm sat}$	$S_{\rm clust}$	$F_{\rm sat,clust}$
$\mu \equiv M_{\rm sat}/M_{\rm cen} \geqslant 0.25$						
$0.30-0.65$	59	0.19 ± 0.05	0.03 ± 0.02	0.16 ± 0.05	0.03 ± 0.03	0.16 ± 0.06
$0.65-0.88$	62	0.21 ± 0.05	0.04 ± 0.02	0.18 ± 0.05	0.05 ± 0.03	0.17 ± 0.06
$0.88-1.02$	61	0.12 ± 0.04	0.04 ± 0.02	0.08 ± 0.04	0.03 ± 0.02	0.09 ± 0.04
$1.02-1.30$	56	0.13 ± 0.05	0.02 ± 0.02	0.11 ± 0.05	0.01 ± 0.02	0.12 ± 0.05
$\mu \equiv M_{\rm sat}/M_{\rm cen} \geqslant 0.1$						
$0.30-0.65$	59	0.24 ± 0.06	0.06 ± 0.03	0.19 ± 0.07	0.06 ± 0.03	0.19 ± 0.07
$0.65-0.88$	62	0.32 ± 0.06	0.07 ± 0.03	0.27 ± 0.07	0.09 ± 0.04	0.25 ± 0.07
$0.88-1.02$	61	0.21 ± 0.05	0.07 ± 0.03	0.15 ± 0.06	0.08 ± 0.04	0.14 ± 0.06
$1.02-1.30$	56	0.20 ± 0.05	0.04 ± 0.03	0.17 ± 0.06	0.03 ± 0.03	0.18 ± 0.06
$\mu \geqslant 0.01$						
$0.30-0.65$	59	0.44 ± 0.06	0.17 ± 0.05	0.33 ± 0.08	0.18 ± 0.05	0.32 ± 0.08
$0.65-0.88$	62	0.48 ± 0.06	0.20 ± 0.05	0.35 ± 0.08	0.22 ± 0.05	0.33 ± 0.08
$0.88-1.02$	61	0.48 ± 0.06	0.21 ± 0.05	0.34 ± 0.08	0.25 ± 0.05	0.31 ± 0.08
$1.02-1.30$	56	0.36 ± 0.06	0.15 ± 0.05	0.25 ± 0.08	0.14 ± 0.05	0.26 ± 0.08

metallicities are used in the modelling, and the age range available, given the redshift distribution of the sample, allows for more accurate age constraints than with low-redshift systems. A typical example, SHARDS123624.42+621454.1 (z=0.639) is presented in Fig. 5. The colour image is a $30'' \times 30''$ RGB composite combining the F606W, F775W and F850LP passbands from the *HST*/ACS GOODS-N images[1]. The red circle extends over a projected radius of $100h_{70}^{-1}$ kpc. The central system is a 2.9×10^{11}M$_\odot$ spheroidal galaxy, surrounded by two close companions. The low-resolution SHARDS spectral energy distribution of host and companions is shown on the left, along with ($1\,\sigma$) error bars. The model best fit is given for each galaxy as a red shading. The best fit ages are also included in each diagram.

2.5 Final Clean-up

The preliminary set of 285 massive galaxies is visually inspected, using the publicly available *HST*/ACS images. The objects are classified as "unresolved" (i.e. PSF-like); spheroidal (including both E and S0 morphologies); disc; irregular/merger and artefacts in the selection (usually spurious detections next to a bright star). The artefacts were removed from the catalogue, and the borderline-unresolved sources were inspected in more detail, removing those that are stars. By comparing the best fits from stellar population synthesis (see sect. 2.3) with a QSO template (Vanden Berk et al. 2009) or a set of stellar spectra (Pickles 1998); we found that all "unresolved" objects brighter than $K_{\rm AB} < 17.5$ (8 found in our sample) were better fit by a QSO spectrum, and, therefore, removed from the final catalogue. The final set comprises 238 massive galaxies: 48% are spheroidal/unresolved; 45% are disk-like; 7% have a merger/irregular morphology. The sample of massive galaxies has 224 systems with an available spectroscopic redshift, allowing us to asses for this subsample an accuracy of $|\Delta z|/(1+z) = 0.46\%$ (median), when using photometric redshifts.

[1] `http://archive.stsci.edu/prepds/goods/`

3 SELECTION OF HOST-COMPANION PAIRS

For each of the 238 massive galaxies, we define merger progenitors as those with a nearby satellite. In this paper, a galaxy is considered a close companion if it is located at a projected distance $\Delta r_\perp \leqslant 100h_{70}^{-1}$ kpc, with a redshift difference $|\Delta z| \leqslant 0.011 \times (1+z)$, i.e. within the $2\,\sigma$ uncertainty of the photometric redshift estimates. We decided to extend the interval in redshift to $2\,\sigma$ because of the high accuracy of the photometric redshifts, in constrast with previous works. We note that 38% of the companions have a spectroscopic redshift, from which we derive a photometric redshift accuracy of $|\Delta z|/(1+z) = 0.75\%$ (median). In order to assess the contamination from foreground/background sources because of the use of photometric redshifts, we follow the methodology laid out in Mármol-Queraltó et al. (2012) (see their §§3.1). In a nutshell, a Monte Carlo method is applied, where mock catalogues are generated by randomly placing massive galaxies within the survey volume, keeping the same redshift distribution as the original catalogue. The fraction of companions is computed for each mock sample. We find that the Monte Carlo runs give convergent fractions within the error bars after 1000 realizations. The fraction of simulated galaxy pairs is defined as $S_{\rm simul}$. We can use this distribution to correct for the effect of contaminants in the true sample (see Mármol-Queraltó et al. 2012, for details). If $F_{\rm obs}$ is the observed fraction of close companions, the corrected one ($F_{\rm sat}$) is:

$$F_{\rm sat} = \frac{F_{\rm obs} - S_{\rm simul}}{1 - S_{\rm simul}} \quad (2)$$

Tab. 3 shows the fraction of massive ($\log M_s/M_\odot > 11$) galaxies with nearby satellites, for three different choices of the stellar mass ratio between companion and host, $\mu \equiv M_{\rm comp}/M_{\rm host}$. We include in the table the results corresponding to the Monte Carlo simulations to account for spurious pairs. Note that this correction stays at the level of ∼5% for pairs with $\mu \geqslant 0.1$ and ∼20% for $\mu \geqslant 0.01$. The 68% (1σ equivalent) error bars are derived from a binomial distribution, following the favoured beta distribution generator presented in Cameron (2011). In addition, we need to take into account the effect of clustering. We perform a similar estimate of the frac-

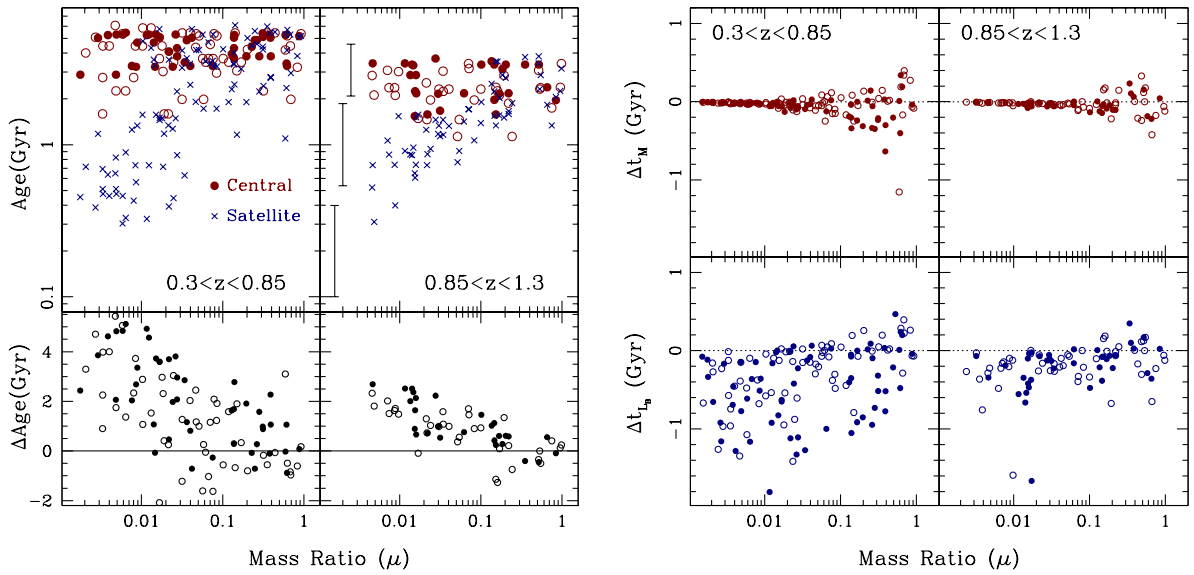

Figure 7. *Left:* Age difference between host (red circles) and companion galaxies (blue crosses) for the exponentially decaying (τ) models. The centrals are split with respect to visual morphology (solid circles for E/S0; open circles for disc/irregular). The top panels show the individual ages, the bottom panels show the age difference between them. The sample is split at the median value of the redshift distribution. *Right:* Rejuvenation of the central galaxy assuming the close companion eventually merges with it. The age difference, $\Delta t \equiv$Age(After Merger)$-$Age(Before Merger), is weighted with respect to the stellar mass content (top) or the rest-frame B-band luminosity (bottom). The sample is split with respect to redshift at the median of the distribution.

tion of companions, as described above, for a set of annuli from $100h_{70}^{-1}$ kpc – which is the fiducial maximum distance chosen in the paper for the selection of pairs – out to $500h_{70}^{-1}$ kpc, at fixed solid angle per annulus, equivalent to the search area. Measurements in the field would yield no significant variation in the number of galaxy pairs over this range, whereas a highly clustered environment would display a monotonic decrease of the number of satellites with increasing radius. We define the environment-corrected value of $F_{\rm sat}$ as the one corresponding to $500h_{70}^{-1}$ kpc, including an error bar determined by the RMS scatter of the satellite fraction between $400h_{70}^{-1}$ and $500h_{70}^{-1}$ kpc. These results are quoted under the column named $S_{\rm clust}$ in Tab 3. The last column ($F_{\rm sat,clust}$) gives the final result of our environment-corrected fraction of satellites, taking into account the effect of clustering. Note the increase in the clustering fraction around z$\sim 0.8-0.9$, where a structure is evident in the redshift distribution of the sources towards the GOODS-N region. The final fraction of satellites is found not to depend on redshift within the range covered, with $F_{\rm sat,corr} = 0.19 \pm 0.08$ (1:10) and 0.31 ± 0.08 (1:100). This trend is in good agreement with Mármol-Queraltó et al. (2012). Figure 6 shows a comparison of our results with recent estimates of the merger fraction of massive galaxies from the literature. All merger fractions correspond to the same search criterion in projected distance, namely $\Delta r_\perp \leqslant 100h_{70}^{-1}$ kpc. In those estimates where the search radius was smaller (typically 20-30 kpc) , a scaling factor was included, according to how much the fraction changes in our sample between these two choices. This correction is compatible with the variations observed by López-Sanjuan et al. (2011). Note that for major mergers (*top*), the increase at high redshift is mainly evident from the larger sample of close pairs in COSMOS (López-Sanjuan et al. 2012), and the high redshift sample of Bluck et al. (2012). Our sample constrains best the evolution of the minor merger ($\mu > 0.01$) fraction, which, in combination with the SDSS data (Ruiz et al., in preparation), suggests no redshift evolution in the fraction of 1:100 minor mergers out to z $\lesssim 1.3$. Regarding the morphology of massive galaxies with satellites, we find a similar distribution as with respect to the parent sample of massive galaxies: 49% of the massive galaxies with satellites have an early-type morphology. In contrast, massive galaxies with a late-type morphology account for 39% of the sample of systems with satellites, and irregulars constitute the remaining 12%.

3.1 Border Effects

In order to assess the effects of the edges of the SHARDS footprint, we consider the number of sources within an aperture with radius R=120 arcsec centered in each of the massive galaxies selected in our sample. This choice represents the worst case scenario: a $500h_{70}^{-1}$ kpc aperture extends over an angle between 60 and 112 arcsec for the redshift range probed by our sample. We compare the number of SHARDS-detected sources, irrespective of redshift, between the massive galaxy under consideration, and the average obtained from 500 random positions within a region always inside the SHARDS footprint (see Fig. 2 of Pérez-González et al. 2013). Only for 9 out of the 238 massive galaxies ($\lesssim 4\%$) a correction is needed at the level of $\sim 8 \pm 6\%$. For the fiducial $\Delta r_\perp = 100h_{70}^{-1}$ kpc chosen to define nearby satellites, border effects are negligible, with none of the massive galaxies requiring a correction.

4 THE AGES OF THE PROGENITOR MERGERS WITH MASSIVE GALAXIES

The top panels of Fig. 7 (*left*) show the ages of host (red circles) and companions (blue crosses) against the stellar mass ratio. The sample is split with respect to redshift. The hosts with a spheroidal

morphology are shown as solid circles, and disc or irregular morphologies are shown as open circles. Characteristic error bars for the stellar age are given on the top-right panel for reference. The bottom panel shows this result as an age difference between host and companion, with the symbol notation representing morphology as in the top panels. There is a subtle, but noticeable difference in the ages of the host galaxies with respect to morphology. Notice the strong trend between age difference and mass ratio. Minor mergers – below 1:10 – have an age difference larger than ∼1 Gyr, except for a few pairs. This trend is consistent with the findings of Mármol-Queraltó et al. (2013), although we note that in the present study we have a higher constraining power on stellar ages from the use of the SHARDS photo-spectra.

Fig 3 showed that a population of very old and low-mass galaxies could affect the completeness level of the sample, and thus the conclusions drawn here. To test this issue further, we compared the age difference between host and companion (Fig. 7, left), with respect to the apparent magnitude of the satellite galaxy. No significant excess of old satellites is found as we probe fainter fluxes. For instance, taking $\Delta\mathrm{Age} < 1\,\mathrm{Gyr}$ to define the fraction of systems with older satellites, we find 36% of pairs with older satellites over the $K_{\mathrm{AB}} = 22 - 23.5$ range, and 16% at $K_{\mathrm{AB}} = 23.5 - 25$. If a bias were present, we would have expected an *increase* of the fraction of older companions towards fainter fluxes. Therefore, no such bias is expected in the derivation of the age difference down to mass ratios $\mu \sim 0.01$.

Is the trend between age difference and mass ratio of Fig. 7 a trivial extension of the strong correlation between mass and age? (see Fig. 4). We explore this issue by using the rank of the age of the satellite galaxies: for a given pair, we compare the age of the satellite with the distribution of stellar ages of galaxies with similar stellar mass and redshift. The rank of the chosen satellite within this distribution tells us whether it is significantly older/younger than similar types of galaxies. The average rank is $59 \pm 28\%$ without any significant variation with respect to redshift or mass ratio, confirming that the observed age difference is the expected one from the mass-age correlation of Fig 4. In other words, the ages of our satellites do not have any systematic variations caused by (or related to) their being in close proximity to a more massive galaxy.

Fig. 7 (*right*) shows the amount of rejuvenation of the central – if the satellite is assumed to eventually merge with it – weighted with respect to stellar mass (top) or rest-frame B-band luminosity (bottom). The rejuvenation age is defined here as:

$$\Delta t_w = t_{\mathrm{AFTER,w}} - t_{\mathrm{CEN,w}} = \frac{w_{\mathrm{SAT}}}{w_{\mathrm{SAT}} + w_{\mathrm{CEN}}}\big(t_{\mathrm{SAT}} - t_{\mathrm{CEN}}\big) \quad (3)$$

where $t_{\mathrm{CEN}}, t_{\mathrm{SAT}}$ are the stellar ages of central and satellite galaxy, respectively, derived from the analysis, and $w_{\mathrm{CEN}}, w_{\mathrm{SAT}}$ are the weights chosen. A more physically motivated weight is the stellar mass ($w_i = M_{s,i}$, top panels of Fig. 7, right). We also give the luminosity-weighted values, estimated in the rest-frame B-band, i.e. $w_i = L_{B,i}$ (bottom panels). The sample is split at the median redshift. The figure shows that the effect of these mergers is relatively unimportant for the merged system, with age differences below ~ 1 Gyr in the majority of the close pairs, even when weighted with respect to luminosity. This result is consistent with the overall old stellar populations found in nearby massive galaxies (see, e.g., Thomas et al. 2005; de la Rosa et al. 2011).

Finally, we explore the impact of environment in our results. We define N_{500} as the number of galaxies with $M_s \geqslant 5 \times 10^9 M_\odot$ at a projected distance $\Delta r_\perp \leqslant 500 h_{70}^{-1}$ kpc of a chosen host galaxy, within the accuracy of the photometric redshift (at the $2\,\sigma$ level) $|\Delta z|/(1+z) \leqslant 0.011$. The choice of stellar mass is justified by the completeness level of the SHARDS sample within our redshift range for a large range of stellar populations (see Fig. 3). In our sample, the distribution suggests $N_{500} = 8$ as the value that separates between low and high density. Fig. 8 shows the central/satellite age difference with respect to mass ratio, splitting the sample according to galaxy density (those in high density regions are shown as filled circles). No significant segregation is found.

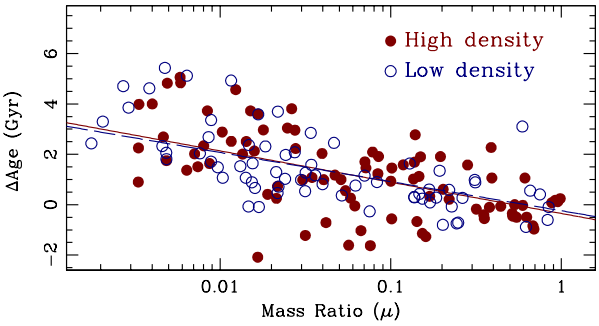

Figure 8. Effect of environment density on the age difference between central and satellite galaxy. Each point corresponds to a massive galaxy from the sample of close pairs. Density is defined for each one as the number of galaxies with stellar mass $M_s \geqslant 5 \times 10^9 M_\odot$, located within a projected distance of $\Delta r_\perp \leqslant 500 h_{70}^{-1}$ kpc inside the redshift accuracy interval. The sample is split at the median value ($N_{500} = 8$) into high (solid red) and low-density (open blue) regions. For reference, the red solid (blue dashed) line traces the least squares linear fit to galaxies in high- (low-) density regions.

5 MASS GROWTH FROM z∼1

The sample presented here can be used to quantify the dominant growth channel of massive galaxies from z∼1. Numerical simulations of structure formation reveal an excess of satellite galaxies (Quilis & Trujillo 2012), with the preferred growth in mergers with a mass ratio around 1:5 (Oser et al. 2012). Fig. 9 (*left*) quantifies the contribution to the growth of massive galaxies as a function of the mass ratio between the satellite and the central galaxy (μ). The histograms with error bars show the fractional contribution of the total mass of the satellites, within each bin in μ, to the *total* stellar mass in centrals. If we assume that all satellite galaxies will be accreted into their centrals by redshift zero, the histogram gives a probability distribution function, P(μ), for the merger growth channel with respect to satellite/central mass ratio, within the redshift range covered (i.e. $\Delta z = 0.3 - 1.3$). This interpretation is applicable when the mass growth rate is relatively constant over this period, a point that is justified below. However, for major mergers such an assumption may break down, given the evolution with redshift claimed by some authors (see, e.g., López-Sanjuan et al. 2012).

From left to right, the panels of Fig. 9 (*left*) refer to the total sample, early- and late-type central galaxies, respectively. Poisson error bars are included. The top panels are log-log plots focusing on the behaviour at the low-mass end, revealing an extended power law. The bottom panels of Fig. 9 (*left*) plot the same histogram with linear-log axes, to show in more detail the region around the peak of the histograms. In order to assess the systematics regarding the selection of spurious pairs, we ran a Monte Carlo simulation where 1000 realizations were made with the positions of the

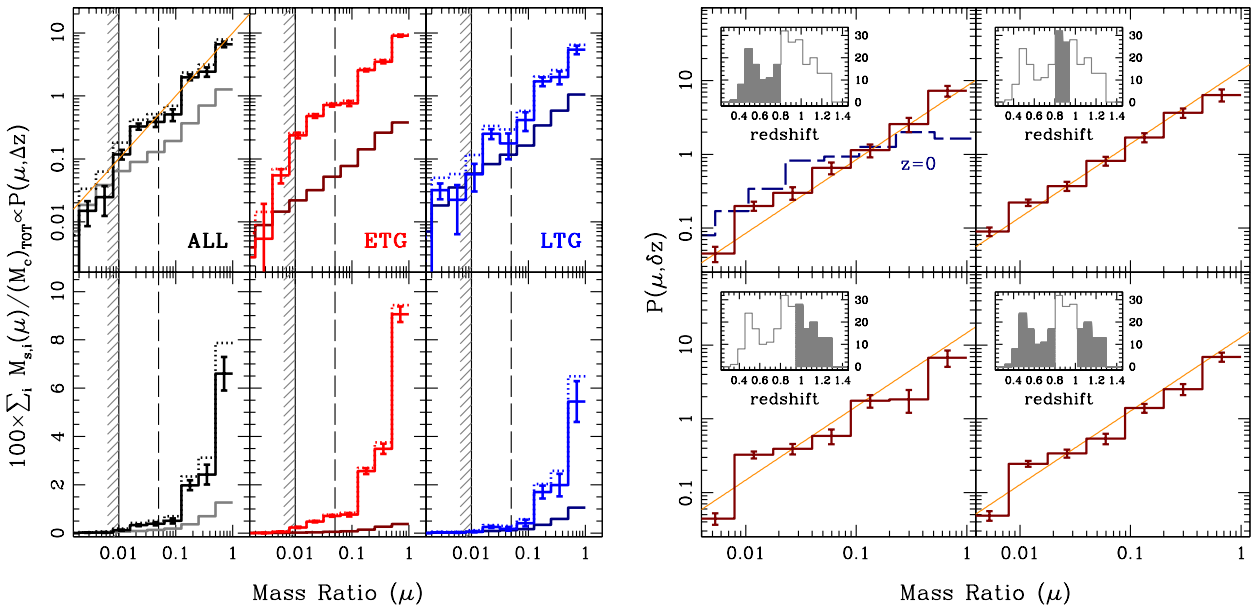

Figure 9. (*Left*): Histogram of the integrated mass fraction contributing to the growth of galaxies as a function of their mass ratio. Along with the complete data set (*left*), The sample is also segregated with respect to the morphology of the central galaxy (early-type galaxies, *middle*; and late-type galaxies, *right*), following the same classification criterion as in Fig. 7. The solid line histograms with error bars correspond to the final values, after applying a correction from the expected background contamination (histograms without error bars). For reference, the uncorrected results are shown as dotted lines. The vertical dashed line marks the conservative 1:20 limit of our sample, and the shaded region marks a more realistic 1:100 limit if we consider that low-mass galaxies are dominated by young stellar populations. For ease of the analysis of the tail and the peak of the distribution, we show log-log plots (*top*) and log-linear plots (*bottom*), respectively. The orange line in the top-left panel is not a fit to the data. It corresponds to a linear increase in the mass fraction (i.e. $P(\mu) \propto \mu$). (*Right*): The distribution is split in several redshift bins. The insets show as a shaded region the redshift range considered in each case. The sample is split in three bins at equal number of massive galaxies per bin. The last panel (bottom-right) shows the full sample, but excluding the redshift range $\Delta z = 0.8 - 1.0$, where an overdensity is evident. The orange lines illustrate the *ansatz* $P(\mu) \propto \mu$. In the low redshift panel, the z=0 blue dashed histogram corresponds to the analysis of massive galaxies from the SDSS of Ruiz et al. (2014).

massive galaxies being moved randomly within the SHARDS footprint. The histograms without error bars correspond to the average of these simulations. The uncorrected histograms, for reference, are also shown with dotted lines. Notice that there is a clear preference towards mass ratios $\mu \gtrsim 0.3$, with a subdominant – although measurable – contribution from minor mergers, that follows a linear scaling with $\log \mu$ (orange line in the top-left panel). The simulations give a different relative contribution with respect to μ, confirming that the observed trend is not a spurious signal from the background distribution of sources. We should emphasize here that the histograms of Fig. 9 are valid on a *relative* sense, i.e. with respect to the different stellar mass ratios, with the assumption that the observed sample provides a faithful representation of massive galaxies over the z $\lesssim 1$ range.

Given that the sample only extends over a relatively small area (130 arcmin^2), we explore the effect of cosmic variance by slicing the catalogue in three redshift bins with equal number of massive galaxies per bin (Fig. 9, *right*). An additional panel (bottom-right) also shows the effect of removing from the sample those galaxies within the overdensity at $z \sim 0.8$. In all cases there is a clear preponderance of major mergers, in agreement with the trend shown in Fig. 9 (*left*). We also estimate the uncertainties from cosmic variance following the prescription of López-Sanjuan et al. (2014, equation 27), which depends on the volume probed, the number density of host galaxies, and the ratio of the number density of host (i.e. massive) galaxies and those sources from which the companion galaxies are extracted (i.e. the general population of SHARDS galaxies). In this case, fluctuations in the pair fraction of order $\pm 15\%$ could be expected from cosmic variance. Such variations are unlikely to change qualitatively our conclusions. The orange lines in Fig. 9 (*right*) – corresponding to the *ansatz* $P(\mu) \propto \mu$ – are fully consistent with our results. For reference, the recent work of Ruiz et al. (2014) based on a large sample of z$\sim$0 massive *elliptical* galaxies from the Sloan Digital Sky Survey is shown in the top-left panel as a dashed blue histogram. Note the significant deficit at z$\sim$0 in the contribution from major mergers. Since the SDSS sample only includes elliptical galaxies, this evolution in the contribution from major mergers is expected to be even more significant for the general population of massive galaxies (Ruiz et al., in preparation).

We derive a simple estimate for the mass growth of massive galaxies over the redshifts probed, by calculating the ratio between the stellar mass in satellites and centrals, within an interval $\Delta t = 2$ Gyr, roughly corresponding to an average merger timescale (see, e.g., Kitzbichler & White 2008). This is meant to be a rough estimate that assumes a constant inflow of satellites with time, as supported by the mild evolution in the fraction of close pairs out to z=1.3 (Tab. 3). Fig. 10 (top) shows the result for the complete sample (red crosses) and the subsample involving only major mergers ($\mu > 0.3$, grey open circles). The measurements include Poisson error bars. Within uncertainties, the mass growth does not change significantly with redshift, with a value around $\tau^{-1} \equiv (\Delta M/M)/\Delta t \sim 0.08 \pm 0.02\,\mathrm{Gyr}^{-1}$. We note that when segregating the sample based on our visual morphological classification of early- and late-type galaxies, no significant difference is

found in their respective mass growth rate. Such a rate would imply a cumulative increase in the stellar mass between z=1 and z=0 of

$$\left(\frac{M_{z=0}}{M_{z=1}}\right) = e^{(t_{z=0}-t_{z=1})/\tau} \sim 1.9 \pm 0.3 \quad (4)$$

For reference, the estimate of van Dokkum et al. (2010), $\Delta \log M/\Delta z = -0.15$, extended out to z=1 gives a mass growth in massive galaxies of a factor ≈ 1.4. We note this result is based on a different approach, namely a comparison of the mass budget at low and high redshift. Our results are also consistent with the $M_{z=0}/M_{z=1} = 1.3$ mass growth factor in the COSMOS field (López-Sanjuan et al. 2012), if we take into account that this estimate extends only to $\mu > 0.1$ mergers, selecting close pairs out to $\Delta r_\perp < 30h^{-1}$ kpc.

In the following, we consider a more realistic estimate of mass growth, by taking into account the merger timescales of close pair systems, which mainly depend on the pair separation and the mass ratio. In Kitzbichler & White (2008) simulated close pairs from the Millennium database were used to derive an estimate of merging timescales, given as a function of pair separation, stellar mass of the central galaxy and redshift. More recently, Jiang et al. (2014) revisited these estimates and proposed an expression that uses the virial masses – given that dynamical friction should be dependent on these – and extend their analysis to lower mass ratios, with an expression where the merging timescale depends linearly on this ratio. Fig. 10 (*bottom*) assumes a merger timescale following the Eq. 7 in Jiang et al. (2014), using the parameterisation of Moster et al. (2010) to convert stellar masses into virial masses, as a function of redshift. Note that no large differences are apparent, within error bars, with respect to the assumption of instantaneous merging (Fig. 10, *top*), because most of the contribution to the mass growth is in major mergers, for which the merging timescales are short. There is a noticeable trend of a diminishing role of major mergers at lower redshift. The relative contribution from major mergers ($\mu > 0.3$) is quite significant, amounting to $71 \pm 8\%$ of the total growth probed by this sample. The analysis of Bluck et al. (2012) of the progenitors of mergers involving massive galaxies at higher redshifts (z=1.7–3) lead to a factor 3 in stellar mass growth, with 65% coming from major mergers. López-Sanjuan et al. (2012) find at $z < 1$ a 75% fraction from $\mu > 0.25$. Our results are fully consistent (see also Tal et al. 2013).

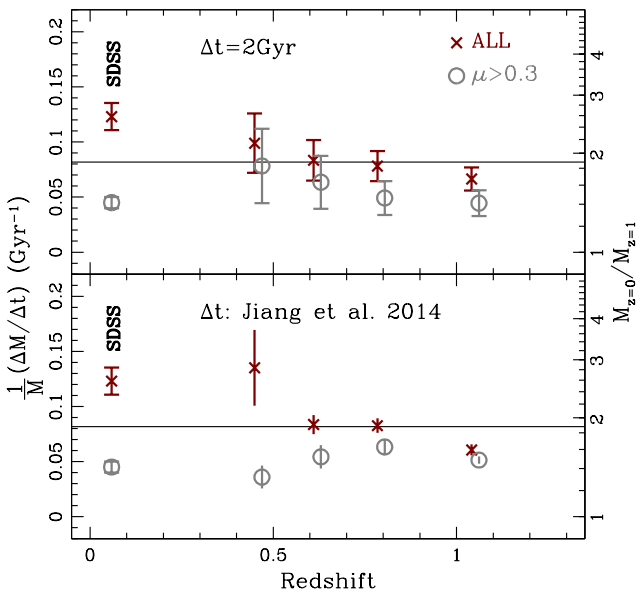

Figure 10. *Top:* Growth rate of massive galaxies with respect to redshift for the simple case of a fixed ($\Delta t = 2$ Gyr) merging timescale. The red crosses (grey circles) correspond to the contribution from the whole sample (only from major mergers, $\mu > 0.3$). The axis on the right gives the expected stellar mass growth between z=1 and z=0 assuming a constant rate. For reference, the points on the left, labelled SDSS, correspond to a nearby sample ($z \sim 0.06$) using the Sloan Digital Sky Survey (Ruiz et al. 2014). *Bottom:* Same as above, although taking into account the dependence of the merging timescale on projected separation and mass ratio, according to the prescription of Jiang et al. (2014).

6 CONCLUSIONS

Satellite galaxies in the region of influence of massive galaxies over a wide range of redshifts provide valuable information about the open question regarding the size growth over the past 8-10 Gyr of cosmic history (e.g. Trujillo et al. 2006, 2007). In this paper we build a sample of massive galaxies from the deep SHARDS dataset. Photometric data from medium band filters allow us both to obtain enough accuracy in the photometric redshift estimates to minimise contamination ($|\Delta z|/(1+z) \sim 0.55\%$, median, confirmed with a spectroscopic sample down to $K_{\rm AB} \sim 24$) and to constrain the age of the stellar populations by use of a large volume of synthetic models. The SHARDS sample is robustly complete over the 0.3<z<1.3 redshift range down to 1:20 if all stellar ages are allowed for, or down to 1:100 if we consider that galaxies with the lowest masses will be significantly younger (Fig. 3).

From the final sample of 238 massive galaxies ($M_s \geqslant 10^{11}$ M$_\odot$), we select those with a nearby companion – at a projected distance $\Delta r_\perp \leqslant 100h_{70}^{-1}$ kpc, and at the same redshift within the ($2\,\sigma$) accuracy of the estimates. The fraction of close pairs is consistent with the results in the literature. However, SHARDS is the first survey capable of probing the evolution of the minor merger rate $\mu > 0.01$ out to $z \sim 1$, with high completeness. In conjunction with the local estimate of the minor merger fraction from the Sloan Digital Sky Survey (Ruiz et al., in preparation), we find no significant evolution in the fraction of 1:100 minor merger progenitors out to z $\lesssim 1.3$ (Fig. 6).

The ages of the stellar populations show a strong correlation with mass fraction between host and companion, with a significant age difference for the more unequal mass mergers (Fig. 7). However, this trend is expected from the general mass-age correlation (Fig. 4), i.e. there is no significant difference between the ages of the companions and the ages of the general population at fixed stellar mass. No significant segregation is observed either when splitting the sample with respect to local density, defined as the number of massive galaxies within a projected distance of $500h_{70}^{-1}$ kpc, and at the same redshift (Fig 8). We emphasize that since massive galaxies are targeted in this study, our sample probes halos where environmental effects should be maximal at those redshifts. Comparing with the results from groups at lower redshift (see, e.g., van den Bosch et al. 2008), our data suggest that quenching in low-mass satellites is not a highly efficient mechanism, and may take significantly longer times, comparable with the lookback times of the systems under study (4–8 Gyr).

The contribution from satellites to the growth of massive galaxies is found to originate mainly from a mass ratio $\mu \gtrsim 0.3$ (Fig. 9), with a net increase to the stellar mass between z=1 and 0

of a factor ~ 1.9, or an average mass growth rate $(\Delta M/M)/\Delta t \sim 0.08 \pm 0.02\,\mathrm{Gyr}^{-1}$, which should be taken as an upper limit to the growth via mergers, as this paper assumes that all central-satellite systems will end up as a merging event. A fraction $\sim 71\%$ of this mass growth is in the form of mergers with a mass ratio $\mu > 0.3$. The combination of age and mass difference in the merger progenitors studied here would imply a rejuvenation of massive galaxies $\lesssim 1\,\mathrm{Gyr}$ over the redshift range probed (Fig. 7). Hence, we find that the dominant channel of mass growth does not introduce any large variations in the age distribution of the stellar material incorporated at $z \lesssim 1$. This result is in agreement with the small radial age gradients observed in massive early-type galaxies at moderate redshift (Ferreras et al. 2009a) and at $z \lesssim 0.1$ (La Barbera et al. 2011, 2012). The small amount of rejuvenation is also consistent with the lack of an age segregation on the mass-size plane (Trujillo et al. 2011).

The observations of merger progenitors over the past 8 Gyr of cosmic time impose strong constraints on models of galaxy formation and evolution. The current "paradigm" seems to converge towards a significant contribution from minor mergers in massive galaxies at $z \lesssim 1$ (see, e.g. Oser et al. 2012; Lackner et al. 2012; Shankar et al. 2013) – mainly finding an explanation to the evolution on the mass-size plane (see, e.g. Naab et al. 2009). However, the observations presented here and elsewhere (see, e.g. López-Sanjuan et al. 2011; Bluck et al. 2012) suggest a substantial revision of the recipes introduced to describe the "baryon physics" in numerical simulations.

ACKNOWLEDGMENTS

We thank Carlos López-Sanjuan for his very valuable comments and suggestions. SHARDS is currently funded by the Spanish MICINN/MINECO with grant AYA2012-31277. Based on observations made with the Gran Telescopio Canarias (GTC), installed at the Spanish Observatorio del Roque de los Muchachos of the Instituto de Astrofísica de Canarias (IAC), in the island of La Palma. The authors acknowledge the use of the UCL Legion High Performance Computing Facility (Legion@UCL), and associated support services, in the completion of this work. IF acknowledges support from the IAC to carry out this research project. EMQ acknowledges the support of the European Research Council via the award of a Consolidator Grant (PI McLure). AH-C acknowledges support from the Augusto González Linares programme (Universidad de Cantabria), and the Spanish "Plan Nacional" grant AYA2012-31447. This work has been supported by the 'Programa Nacional de Astronomía y Astrofísica' of the Spanish Ministry of Science and Innovation under grant AYA2010-21322-C03-02. We have made extensive use of the Rainbow Cosmological Surveys Database, operated by the Universidad Complutense de Madrid (UCM), in partnership with the University of California Observatories at Santa Cruz (UCO/Lick, UCSC).

REFERENCES

Aller, L. H., ed., 1984, Astrophys. Space Sci. Libr. Vol. 112, Physics of Thermal Gaseous Nebulæ . Reidel, Dordrecht
Anders, P. & Fritze-von Alvensleben, U., 2003, A&A, 401, 1063
Arnouts, S., et al. 2007, A& A, 476, 137
Baldry, I. K., Glazebrook, K., Brinkmann, J., Ivezić, Z., Lupton, R. H, Nichol, R. C., Szalay, A. S., 2004, ApJ, 600, 681
Balogh M. L., Morris S. L., Yee H. K. C., Carlberg, R. G., Ellingson, E., 1999, ApJ, 527, 54
Barro, G., et al. 2011, ApJS, 193, 13
Bell, E. F., McIntosh, D. H., Katz, N., Weinberg, M. D., 2003, ApJS, 149, 289
Bell, E. F., et al., 2008, ApJ, 680, 295
Bundy, K., Fukugita, M., Ellis, R. S., Targett, T. A., Belli, S., Kodama, T., 2009, ApJ, 697, 1369
Bluck, A. F. L., Conselice, C. J., Buitrago, F., Grützbauch, R., Hoyos, C., Mortlock, A., Bauer, A. E., 2012, ApJ, 747, 34
Brammer, G. B., van Dokkum, P. G., Coppi, P., 2008, ApJ, 686, 1503
Brammer, G. B., et al., 2011, ApJ, 739, 24
Bruzual G., Charlot S., 2003, MNRAS, 344, 1000
Cameron, E., 2011, PASA, 28, 128
Cardelli, J. A., Clayton, G. C., Mathis, J. S., 1989, ApJ, 345, 245
Cenarro, A. J., Gorgas, J., Vazdekis, A., Cardiel, N., Peletier, R. F., 2003, MNRAS, 339, L12
Chabrier, G., 2003, PASP, 115, 763
Cid Fernandes, R., Mateus, A., Sodré, L., Stasińska, G,. Gomes, J. M., 2005, MNRAS, 358, 363
Conselice, C. J., 2006, ApJ, 638, 686
Cooper, M. C., et al. 2012, MNRAS, 419, 3018
Cowie, L. L., Barger, A. J., Hu, E. M., Capak, P., Songalia, A., 2004, AJ, 127, 3137
Daddi E., et al., 2005, ApJ, 626, 680
de la Rosa, I. G., La Barbera, F., Ferreras, I., de Carvalho, R. R., 2011, MNRAS, 418, L74
de Ravel, L., et al., 2011, arXiv:1104.5470
Faber, S. M., et al., 2007, ApJ, 665, 265
Ferreras I., Lisker T., Carollo C. M., Lilly S. J., Mobasher B., 2005, ApJ, 635, 243
Ferreras I., Lisker T., Pasquali A., Kaviraj S., 2009a, MNRAS, 395, 554
Ferreras I., et al., 2009b, ApJ, 706, 158
Ferreras I., et al., 2012, AJ, 144, 47
Ferreras I., La Barbera, F., de la Rosa, I. G., Vazdekis, A., de Carvalho, R. R., Falcón-Barroso, J., Ricciardelli, E., 2013, MNRAS, 429, L15
Grogin, N. A., et al. 2011, ApJS, 197, 35
Huang, S., Ho, L. C., Peng, C. Y., Li, Z.-Y., Barth, A. J., 2013, ApJ, 768, L28
Hernán-Caballero, A., et al., 2013, MNRAS, 434, 2136
Ichikawa, T., et al., 2007, PASJ, 59, 1081
Jiang, C. Y., Jing, Y. P., Han, J., 2014, ApJ, 790, 7
Koekemoer, A. M., et al. 2011, ApJS, 197, 36
Lotz, J. M., Jonsson, P., Cox, T. J., Croton, D., Primack, J. R., Somerville, R. S., Stewart, K., 2011, ApJ, 742, 103
Kaviraj, S., et al., 2007, ApJS, 173, 619
Kitzbichler, M. G., White, S. D. M., 2008, MNRAS, 391, 1489
Kron, R. G., 1980, ApJS, 43, 305
La Barbera, F., Ferreras, I., de Carvalho, R. R., Lopes, P. A. A., Pasquali, A., de la Rosa, I. G., De Lucia, G., ApJ, 740, L41
La Barbera, F., Ferreras, I., de Carvalho, R. R., Bruzual, G., Charlot, S., Pasquali, A., Merlin, E., 2012, MNRAS, 426, 2300
La Barbera, F., Ferreras, I., Vazdekis, A., de la Rosa, I. G., de Carvalho, R. R., Trevisan, M., Falcón-Barroso, J., Ricciardelli, E., 2013, MNRAS, 433, 3017
Läsker, R., van den Bosch, R. C. E., van de Ven, G., Ferreras, I., La Barbera, F., Vazdekis, A., Falcón-Barroso, J., 2013, MNRAS, 434, L31

Lackner, C. N., Cen, R., Ostriker, J. P., Joung, M. R., 2012, MNRAS, 425, 641
Lin, L., et al. 2010, ApJ, 718, 1158
López-Sanjuan, C., et al., 2011, A&A, 530, 20
López-Sanjuan, C., et al., 2012, A&A, 548, A7
López-Sanjuan, C., et al., 2014, A&A, 564, A127
Mármol-Queraltó E., Trujillo I., Pérez-González P. G., Varela J., Barro G., 2012, MNRAS, 422, 2187
Mármol-Queraltó, E., Trujillo, I., Villar, V., Barro, G., Pérez-González, P. G., 2013, MNRAS, 429, 792
Montes, M., Trujillo, I., Prieto, M. A., Acosta-Pulido, J. A., 2014, MNRAS, 439, 990
Moster, B. P., Somerville, R. S., Maulbetsch, C., van den Bosch, F. C., Macciò, A. V., Naab, T., Oser, L., 2010, ApJ, 710, 903
Naab T., Johansson P. H., Ostriker J. P., 2009, ApJ, 699, L178
Newman, A. B., Ellis, R. S., Bundy, K., Treu, T., 2012, ApJ, 746, 162
Oser, L., Naab, T., Ostriker, J. P., Johansson, P. H., 2012, ApJ, 744, 63
Patton, D. R, Carlberg, R. G., Marzke, R. O., Pritchet, C. J., da Costa, L. N., Pellergini, P. S., 2000, ApJ, 536, 153
Pérez-González P. G., Trujillo I., Barro G., Gallego J., Zamorano J., Conselice C. J., 2008, ApJ, 687, 50
Pérez-González P. G., et al., 2008, ApJ, 675, 234
Pérez-González P. G., et al., 2013, ApJ, 762, 46
Pickles, A. J., 1998, PASP, 110, 863
Quilis, V. & Trujillo, I., 2012, ApJ, 752, L19
Rogers, B., Ferreras, I., Kaviraj, S., Pasquali, A., Sarzi, M., 2009, MNRAS, 399, 2172
Ruiz, P., Trujillo, I., Mármol-Queraltó, E., 2014, MNRAS, 442, 347
Sánchez-Blázquez, P., Forbes, D. A., Strader, J., Brodie, J., Proctor, R., 2007, MNRAS, 377, 759
Shankar, F., Marulli, F., Bernardi, M., Mei, S., Meert, A., Vikram, V., 2013, MNRAS, 428, 109
Tal, T., van Dokkum, P. G., Franx, M., Leja, J., Wake, D. A., Whitaker, K. E., 2013, ApJ, 769, 31
Thomas, D., Maraston, C., Bender, R., Mendes de Oliveira, C., 2005, ApJ, 621, 673
Trujillo I., Ferreras I., de La Rosa I. G., 2011, MNRAS, 415, 3903
Trujillo I., et al., 2006, ApJ, 650, 18
Trujillo I., Conselice C. J., Bundy K., Cooper M. C., Eisenhardt P., Ellis R. S., 2007, MNRAS, 382, 109
Vanden Berk, D. E., et al., 2001, AJ, 122, 549
van den Bosch, F. C., Aquino, D.,Yang, X.,Mo, H. J., Pasquali, A., McIntosh, D. H., Weinmann, S. M., Kang, X., 2008, MNRAS, 387, 79
van Dokkum, P. G., et al., 2010, ApJ, 709, 1018
van Dokkum, P. G., Conroy, C., 2010, Nature, 468, 940
Wang, W.-H., Cowie, L. L., Barger, A. J., Keenan, R. C., Ting, H.-C., 2010, ApJS, 187, 251
Wirth G. D., et al. 2004, AJ, 127, 3121
Xu, C. K., Zhao, Y., Scoville, N., Capak, P., Drory, N., Gao, Y., 2012, ApJ, 747, 85

APPENDIX A: EFFECT OF THE STAR FORMATION HISTORY ON DERIVED PARAMETERS

Tab. 2 shows that three different sets of (standard) grids were chosen to parameterise the star formation histories of galaxies. We show here the differences found between them with respect to stellar age and mass. All three models are explored in the same way, with the same base population synthesis models, i.e. Bruzual & Charlot (2003) models with a Chabrier (2003) initial mass function.

Fig. A1 (*left*) plots the difference between the best fit stellar ages of the three different as a function of stellar mass (*left*) or age (*right*). Note the expected trend towards younger SSP-ages and older τ-model ages. The latter is mainly caused by the tendency of the fitting model to favour small timescales in order to avoid the extended tail of the exponential function (see Ferreras et al. 2012, for a detailed example corresponding to a massive galaxy at high redshift). The grey dots correspond to the general population, whereas the sample of galaxies in close pairs are highlighted as red open circles (host) and blue crosses (lower mass companion). The figure shows that the sample of galaxies in close pairs explored in this paper is representative of the general population, so no systematic bias is expected with respect to the choice of star formation history.

In addition, we present on the right hand side of Fig. A1 the trend between mass ratio and age difference, i.e. the equivalent of Fig. 7 (bottom-left panels) with all three model grids, to confirm that the strong correlation is independent of the parameterisation of the star formation history.

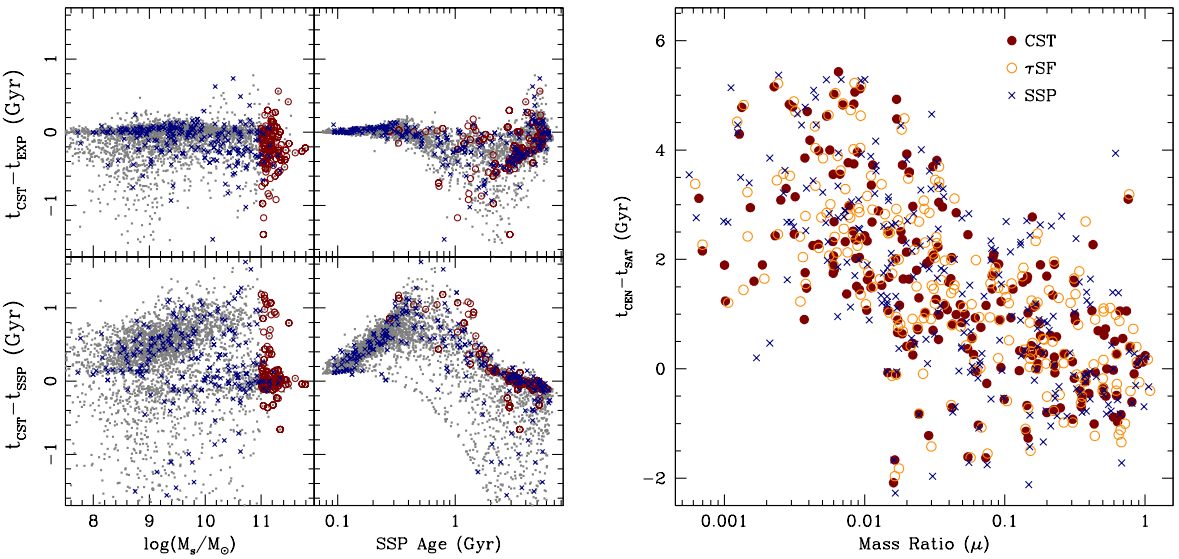

Figure A1. *Left*: Comparison of stellar ages between the three different model grids used in this paper (Tab. 2). The grey dots correspond to the general sample, whereas host (companion) galaxies in close pairs are shown as red open circles (blue crosses). *Right:* Comparison of the correlation between mass ratio and age difference for the three model grids, as labelled.